Design, numerical simulation and experimental testing of a controlled electrical actuation system in a real aircraft morphing wing model

R. M. Botez
ruxandra@gpa.etsmtl.ca
M. J. Tchatchueng Kammegne and L. T. Grigorie
École de Technologie Supérieure
Montréal
Québec
Canada

ABSTRACT

The paper focuses on the modelling, simulation and control of an electrical miniature actuator integrated in the actuation mechanism of a new morphing wing application. The morphed wing is a portion of an existing regional aircraft wing, its interior consisting of spars, stringers, and ribs, and having a structural rigidity similar to the rigidity of a real aircraft. The upper surface of the wing is a flexible skin, made of composite materials, and optimised in order to fulfill the morphing wing project requirements. In addition, a controllable rigid aileron is attached on the wing. The established architecture of the actuation mechanism uses four similar miniature actuators fixed inside the wing and actuating directly the flexible upper surface of the wing. The actuator was designed in-house, as there is no actuator on the market that could fit directly inside our morphing wing model. It consists of a brushless direct current (BLDC) motor with a gearbox and a screw for pushing and pulling the flexible upper surface of the wing. The electrical motor

Paper 4346. Manuscript received 26 January 2015, revised version received 31 May 2015, accepted 12 June 2015.

and the screw are coupled through a gearing system. Before proceeding with the modelling, the actuator is tested experimentally (stand alone configuration) to ensure that the entire range of the requirements (rated or nominal torque, nominal current, nominal speed, static force, size) would be fulfilled. In order to validate the theoretical, simulation and standalone configuration experimental studies, a bench testing and a wind-tunnel testing of four similar actuators integrated on the real morphing wing model are performed.

NOMENCLATURE

B	friction coefficient
$E(s)$	PD position controller transfer function
E_k	induced voltage (back EMF) in the k^{th} winding
F	function in back EMF equation
i_k	current of the kth phase
I	motor current
J	inertia
k_e	angular speed constant
k_t	torque constant
K_c	critical gain
K_e	back EMF constant
K_p	proportional gain in position controller
L	motor inductance
L_k	inductance of the k^{th} winding
P_e	electric power
R	motor resistance
R_k	resistance of the k^{th} winding
T_c	oscillation period
T_d	derivative time constant in position controller
T_e	electromagnetic torque
U	motor voltage
V_{ik}	line-to-line voltage
V_k	voltage of the k^{th} phase
w	motor angular speed
θ	electrical rotor angular position
ω	rotor speed
EMF	electromagnetic force
MSES	computer fluid dynamic code developed by Professor Mark Drela from MIT

1.0 INTRODUCTION

The idea of changing the wing shape configuration or geometry has been studied since the 19th century. The Wright brothers' aircraft was able to do roll control by changing the twist of its wing using cables actuated directly by the pilot(1). Currently, there are a lot of morphing aircraft studies, developed by industrial entities or by different universities in their research labs.

Green aviation policies have driven the trend to replace air-driven and hydraulic-type transmission devices by motor-driven equipment(2). Employing a miniature electrical actuator with an integrated BLDC motor makes it possible to control the shape of an aircraft wing in real time with the morphing wing technique. Thanks to morphing technology, it is possible to optimise wing performance at all flight conditions and for each flight segment.

A brushless direct current (BLDC) motor is a synchronous rotary machine controlled by electronic commutation. Its rotor is a permanent magnet with an integrated position sensor that senses the rotor position. The induced voltage in the motor winding (back EMF) has a trapezoidal waveform. A BLDC motor with its trapezoidal induced voltage waveform has the starting characteristics of a direct current rotary machine(2). BLDC motors are widely used in aerospace, household appliances, automation and industrial process control. The use of this type of electrical rotary machine is extensive and is growing due to its small size, high efficiency, large torque, long lifetime and low noise, and because it performs commutation electronically. This last feature is particularly interesting for aerospace industries because commutation does not cause any chance of sparks occurrence. BLDCs, therefore offer a high level of safety and reliability in addition to their other advantages.

In 2000, researchers at the University of Stuttgart proposed a new method to develop the morphing concept(3). Their approach consisted on using of a shock control bump inflated with air, while the objective was to minimise the negative effects of shockwaves in transonic flow. The numerical results showed a 70% decrease in the wave drag and a 15% decrease in the wing total drag. A comparative study between the drag reduction obtained with the developed approach and with the approach using a higher polynomial contour bump, was performed(3). Considering aerodynamics and structural requirements, researchers from the Institute for Control Engineering and from the Institute for Aerodynamics and Gas Dynamics in Stuttgart, Germany, used a new approach to design an adaptive shock control bump(4). In this way, an optimisation method to generate optimal shock control bump contour for a given height and position was developed. The proposed concepts were validated by using a small scale demonstrator(4).

A 10% drag reduction for Mach numbers between 0·72 and 0·77 was found in similar studies developed by the researchers of the DLR German Aerospace Research Establishment(5). A shape modification concept for transonic wing sections using both MSES (Euler + boundary layer) code and Navier/Stokes code showed an improvement of the lift-to-drag ratio. For the MSES code 15% of the lift-to-drag ratio and 8·3% for the Navier/Stokes improvement was observed(6).

In an overview of the research at NASA Langley research center, analytical and experimental results, plans, potential technology pay-offs, and challenges were discussed in order to develop the enabling technologies to actively and passively control aircraft and rotorcraft vibration and loads using smart devices(7). Also, in another overview in which NASA morphing program is focusing on multiple disciplinary research for the development of the smart technologies so as to use them for the improvement of the state-of-the-art aircraft systems, research and development pertinent to self-adapting airframe systems, advanced piezoelectric materials, advanced fibre optic sensing techniques have been exposed(8).

In 2001 Stanewsky presented a summary of flow control methodology and adaptive wing technology, along with a discussion of the aerodynamic contributions to adaptive wing concepts of varying complexity(9). In 2007, a new principle of morphing was presented based on a dielectric electroactive polymer (EAP) skin using micro fiber composite actuators(10). Because the EAP skin could not be sufficiently pre-loaded, a rubber skin was used in the experimental testing. In another study developed at University of Virginia in 2003, a cellular metal vertebrate structure which relies on the SMA to achieve fully reversing shape change, when these are combined with flexible face sheets a load bearing morphing panel was developed(11). In 2006, a researcher from the Aeronautics and Astronautics Department, Purdue University, US, contributed a review of fixed wing aircraft implementing morphing techniques(12). Various alternatives of morphing aircraft were exposed and discussed, as well as the associated design techniques and fabrication technologies. Also, an analysis of the four basic elements used in a morphing wing structure has been performed: sensors to measure positions, control systems to convert the measurements into an activation signal, actuation mechanisms to provide mechanical motion and precise positioning, and efficient power sources to drive actuation(12). Recent work in smart materials and adaptive structures is providing researchers the opportunity to investigate how this adaptive structure can be used to morph the aerofoil shape(13). The most common characteristics of some smart materials used in adaptive structures are listed in Table 1(13): the maximum strain (Max. strain) – allowable normalised deformation expressed in percent; the maximum stress (Max. stress) – allowable stress expressed in MPa; the elastic energy density (the potential energy stored in a small volume element upon deformation) expressed in J/g; maximum efficiency (Max. effic.), representing the maximum value of efficiency (determined for specific smart materials as a function of the ratio of recovery stress to yield stress), and expressed in percent; the relative response speed (is the speed reaction of the material when submitted to an external disturbance).

Table 1
Smart materials and their characteristics(13)

Material	Max strain (%)	Max. stress (MPa)	Elastic energy density (J/g)	Max. effic.(%)	Relative speed
Electrostrictor Polymer P (VDF-TrFE)	4	15	0·17	–	Fast
Piezoelectric Ceramic (PZT)	0·2	110	0·013	>90	Fast
Single Crystal (PZN-PT)	1·7	131	0·13	>90	Fast
Polymer (PVDF)	0·1	4·8	0·0013	n/a	Fast
SMA (TiNi)	>5	>200	>15	<10	Slow

Among the materials compared in Table 1, shape memory alloy (SMA) appears to be a good candidate to use for flexible skin morphing. Among smart materials, SMAs can produce rather large plastic deformations.

The design of a new flap architecture using compliant (SMA) ribs for a variable-camber trailing edge was assessed. Upon activation of the SMA, the ribs were able to change the camber's morphology. In addition, a numerical optimisation process, incorporating practical constraints and finite element (FE) analysis were also performed, in order to evaluate the structural design and the aero-structural performance(14,15). Another study used SMAs in morphing flap actuation, controlled by robust non-linear controllers. These flaps were fabricated in ultra-light scaled models made of balsa wood and nylon sticks, utilising their high strength and low weight characteristics(16). The use of SMA wires as actuators for wing flaps was submitted to wind-tunnel testing. The trailing edge was morphed by means of six SMA wires that could pull the flap assembly upon electrical activation, while ten springs acted to regain the initial wing configuration when the SMA wires cooled down(17). A wing prototype with flexible skin made of fibreglass composite and a rubber sheet was manufactured and tested. SMA was used to change the shape of the flexible skin(18). Torsion bars and SMA wires controlling the roll of a morphing wing model aircraft have been tested in both a wind tunnel and during flight(19).

Also, the SMA behaviour has been modelled according to the model proposed by Liang and Rogers model, simulation results being presented in terms of output displacements and morphed shape(20). Linear actuators incorporated in statically determinate structure around which a prototype aerofoil has been built, were used for morphing, finally the prototype aerofoil was tested in the wind tunnel to analyse drag reduction.

In 2009, a study investigated and presented an overview of smart material application(21). The investigation focused essentially on shape memory alloy as actuator in order to change the camber of the aerofoil. Subsequently, an adaptive aerofoil was designed with the aim of changing the camber of the aerofoil during cruise conditions(22); different aerofoils shape was predicted with the help of finite element analysis.

Based on results provided by a finite element method(18), a wing prototype was manufactured with a specially-designed position control for wing trailing-edge deflection(23). This control system produced a minimum of 5mm trailing-edge deflection. Experimental wind-tunnel tests showed that the lift-to-drag ratio was improved at a very low angle-of-attack variation (cruise conditions) and decreased by increasing the angle-of-attack(23).

The researchers from the Department of Mechanical Engineering, Temple University, Philadelphia, used smart materials to control the flap setting of a given aircraft(24). One end of the actuator was attached to the wing box and the other was attached tangentially to a rotating cylinder fixed to the flap. The deflection of the flaps was achieved by arranging the SMA springs in an upper and lower layer. A three-way switch was utilised to apply current to the springs. Depending on how and where the current was applied, the flap's deflection was either upward or downward. Wind-tunnels tests were carried out at the tunnel outlet in order to demonstrate the feasibility of the design concept.

Another project used a camber change to modify the aerofoil shape, based on SMA as actuator(25). A design optimisation method was used to generate different aerofoil design solutions. The optimisation method utilised the aerodynamic properties of the aerofoil to optimise the design problem and to maximise the lift-to-drag ratio for the aerofoil shape.

The chord wise air collection method was used to implement a laminar flow control over the upper surface of a wing(26). That method was used to change the transition location moved to a desired location, which was then maintained with the help of a numerical algorithm(27). Three tasks are involved in moving and maintaining the transition location: keeping the lift and the pitch moment coefficients constant, and wing optimisation by reducing the kinetic energy and drag coefficient(28).

Morphing wing realisation based on maintaining the desired turbulence level over a flat plate equipped with a suction porous panel, was done at Southampton University. The degree of turbulence was evaluated by computing the Root Mean Square (RMS) of the pressure signals(29). To control the wing shape by modifying its trailing-edge, an actuation mechanism system was designed and tested. The goal of the actuation mechanism was to transmit its rotary motion to the rib aiming to realise the target optimised shape(30,31). A control system with the aim to control the shape of a camber trailing edge was proposed in Ref. 32. A servo motor integrated inside the wing was installed in order to modify the shape changing of the trailing edge when it was actuated. The optimised trailing-edge shape was stored into a database. Through strain sensors installed on the trailing edge the measured shape was reconstructed and compared with the optimised aerofoil shape stored in the database. Two control strategies (open and closed loop) were investigated. An SMA model has been developed in Matlab and simulation has been carried out to control the laminar to turbulent flow transition point towards the trailing edge of the aircraft(33).

A closed loop control based on the fuzzy technique was developed to control the transition point during real time testing in a Canadian project(34). Also, in the same project, an on-off and

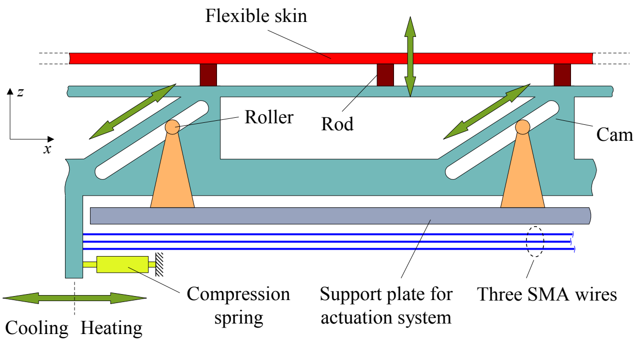

Figure 1. Actuation mechanism concept in CRIAQ 7.1 research project.

proportional-integral controller to morph a flexible skin was designed and tested(35,36), and a numerical analysis and the experimental validation of a hybrid controller based on fuzzy logic and a Proportional-Integral-Derivative (PID) algorithm to ensure SMA actuator displacements were performed(37,38). PID controller has been used to control the SMA based actuator (see Fig. 1) in order to control the laminar to turbulent transition point for drag reduction. Transfer function was developed in Simulink and used to approximate the PID gains using Zeigler Nichols method. The team developed also some adaptive neuro-fuzzy inference system-based controllers for smart material actuator modelling(39,40). The controllers were designed to correlate each set of forces and electrical currents applied to the actuators.

LQR control has been used to calculate the optimal aerodynamic forces and the command forces are fed into the fuzzy logic controller that produces required control surface deflection under the preset rules defined by the morphing deflection controller, this work shows a successful tracking of an arbitrary flight path using a hybrid LQR-neuro fuzzy control scheme(41).

Despite the progress in smart materials technology, their high power consumption, requiring a heavy power system, has limited their utilisation in aerospace(35-38). To address this issue, a new aerofoil shape-changing concept utilising an electrical actuator was proposed in 2014(42). The electrical actuator is a direct current motor. Lightweight actuators are part of the trend in green aviation. Maximising the integration of electrical systems in future aircraft will reduce their weight. Using electrical actuators, such as DC motors, will bring multiple benefits in addition to those gained by morphing, because such actuators are lightweight, can be easily integrated into a system, and need less power than smart materials.

A wing prototype with an integrated actuation mechanism was fabricated and tested at the Ecole

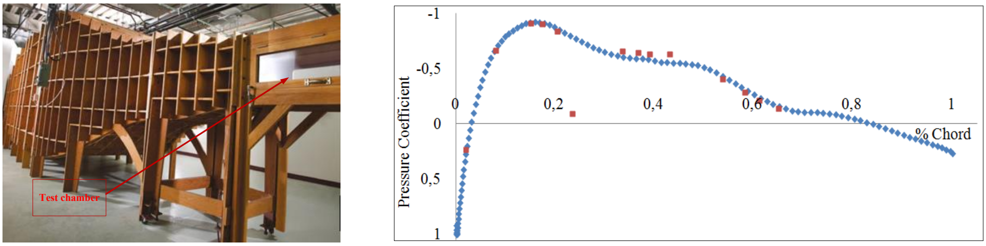

(a)

(b)

Figure 2(a). Price-Païdoussis subsonic wind tunnel; (b) Comparison between theory and wind-tunnel experiments for a morphing wing.

de Technologie Superieure in Montreal, Canada. The actuator position was controlled using a cascade control algorithm. Wind-tunnel tests were carried out to verify the predicted aerodynamic response. Figure 2(a). shows a complete view of the Price-Païdoussis wind tunnel used for those tests(43), while Fig. 2(b). shows that the measured pressure coefficient curve (red) is very close to the curve of the predicted coefficients (blue)(42).

The work presented here describes a new morphing wing application developed by using an actuation mechanism based on some miniature high-force in-house developed electrical actuators. In the following sections the paper exposes: (i) the morphing wing project background, including the architecture of the proposed actuation system, (ii) the theoretical analysis of the BLDC motor and its gearbox, contained in the developed electrical actuator; (iii) the actuator control system design (the current controller and the position controller); (iv) experimental results obtained in the morphing wing bench test and wind-tunnel test actuation.

2.0 MORPHING PROJECT BACKGROUND

In this research project, realised at the Ecole de Technologie Supérieure in Montréal, Canada in collaboration with Thales, Bombardier Aerospace, École Polytechnique, National Research Council Canada (IAR-NRC), and also with Italian researchers from University of Naples Frederico II, CIRA and Alenia, a wing-aileron prototype is designed, tested and validated using wind-tunnel tests at the National Research Council Canada (IAR-NRC). The project is a multidisciplinary one, the involved entities working together; the research team is divided into three sub-teams covering aerodynamic, structural, and control fields. The project aims to reduce the operating costs for the new generation of aircraft through in-flight fuel economy, and also to improve aircraft performances, expand its flight envelope, replace conventional control surfaces, reduce drag to improve range and reduce vibrations and flutter risk. To achieve these purposes, two particular objectives for our team (Research Laboratory in Active Controls, Avionics and Aeroservoelasticity (LARCASE) of the Ecole de Technologie Supérieure in Montréal, Canada) were established in this project: (1) to detect and visualise airflow characteristics using pressure sensors installed on the upper surface of the morphing wing; and (2) to develop a system for active control of the morphing wing during flight to move the transition point from laminar to turbulent flow closer to the trailing edge, thereby promoting large laminar regions on the wing surface, and thus reducing drag over an operating range of flow conditions univocally defined by mean of Mach numbers, airspeeds, and angles-of-attack.

To be more specific to a real morphing application, the wing used in this project is a full-scaled portion of the wing of a regional aircraft (Fig. 3(a)), having maximum chord of 1·5m, and a

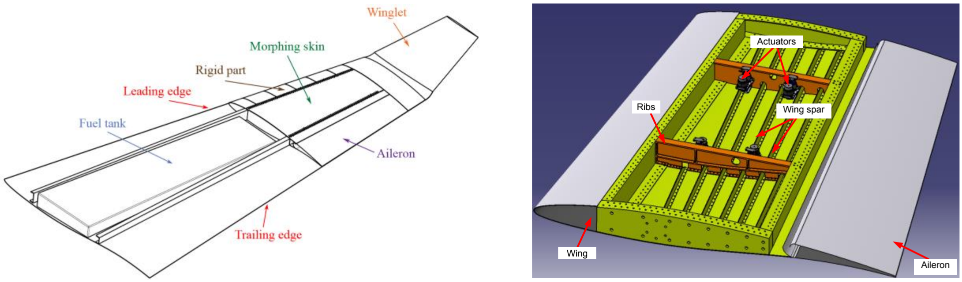

(a) (b)

Figure 3. Used wing as a full-scale portion of regional aircraft wing.

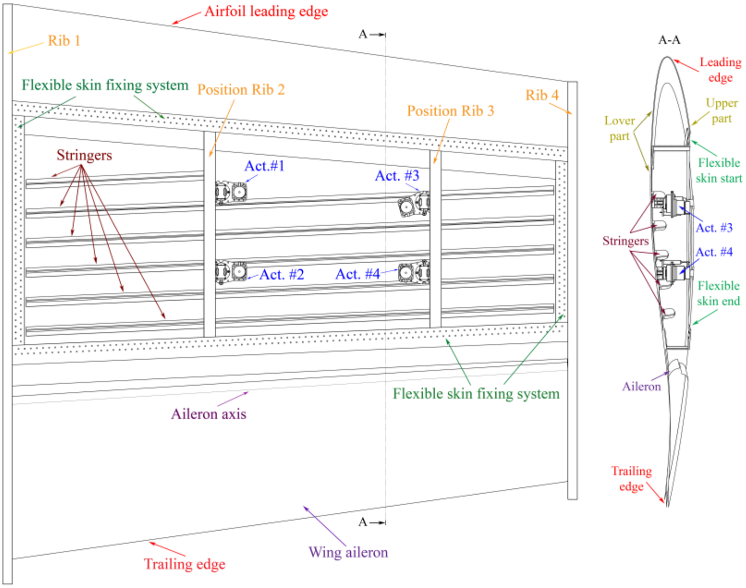

Figure 4. Wing structure and actuations lines positions.

minimum one of 1·08m. It consists of wing spars, ribs and an aileron (Fig. 3(b)).

In a preliminary aerodynamic study, 74 optimised aerofoils were calculated by modifying the reference aerofoil for each airflow condition as some combinations between 15 angles-of-attack (–3°, –2·5°, –2°, –1·5°, –1°, –0·5°, –0·25°, 0°, 0·25°, 0·5°, 0·75°, 1°, 1·25°, 1·5°, 2°), two Mach numbers (0·15, 0·25) and 14 aileron deflection angles (between –7° and 7°, due to the constraints imposed by the wind-tunnel aerodynamic balance). The optimised aerofoils were found through numerical simulations by the aerodynamic team, using some Computer Flight Dynamic (CFD) software and optimisation algorithms.

The experimental wing model has three parts: (1) a metal part coming from the original aircraft wing, with unmodified structure, able to sustain the wing loads; (2) a morphing part, consisting of a flexible skin installed on the upper surface of the wing; and (3) an actuated aileron, designed starting from the original one on the aircraft (Fig. 4). The metal part structure contains four ribs, two at the ends (Rib 1 and Rib 4), and two inside (Rib 2 and Rib 3) having also the role to support the actuators.

The morphing part is actuated by four similar electric actuators, placed on two actuation lines at 32% (Act. #1 and Act. #3), respectively 48% (Act. #2 and Act. #4) from chord (Fig. 4). For each of the 74 optimised aerofoils resulted four vertical displacements corresponding to the positions of the four actuators (Fig. 5), stored in a database in order to be used as reference vertical displacements for the control system. Therefore, the morphing shape control is achieved by controlling the actuators' positions.

Two control architectures are planned to be developed: (1) an open loop architecture, controlling the morphing wing system and the aileron deflection angle, and (2) a closed loop architecture, which includes the open loop architecture as an internal loop and controls the transition point position based on the information from the pressure sensors installed on the flexible skin and on the aileron upper surface. A grid of the theoretical (optimised) displacements for all four actuators,

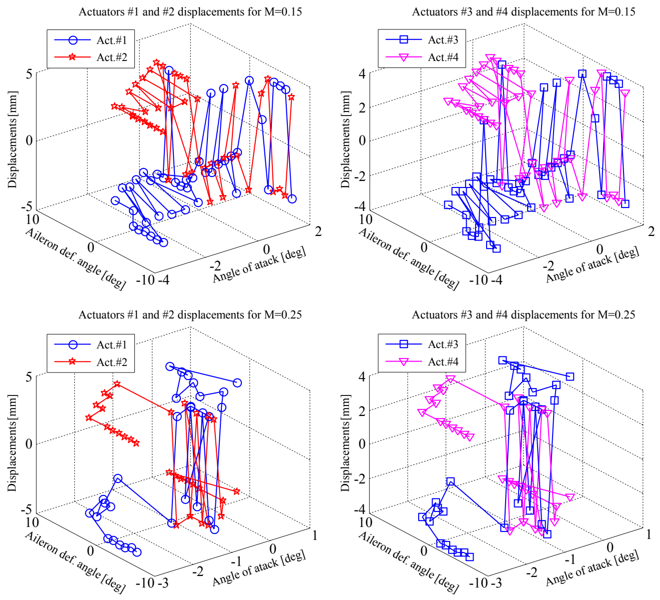

Figure 5. Actuators displacements for Mach = 0·15 and Mach = 0·25.

for Mach = 0·15 and Mach = 0·25, is shown in Fig. 5.

The project actual status refers only to the open loop control architecture at the level of the morphing system actuation: design, numerical simulations and experimental testing. In the open loop architecture the pressure sensors are used just to visualise the transition point position in the wind-tunnel tests, and validate in this way the theoretical aerodynamic optimisation process for all 74 optimised aerofoils; 32 Kulite pressure sensors are planned to be installed on the flexible skin, while other 8 are planned to be installed on the upper surface of the aileron.

The current paper extends the studies realised by Kammegne *et al*. at Ecole de Technologie Superieure in Montreal$^{(42)}$, but, instead of using a mechanical system to convert the rotary motion of the actuator into a vertical displacement, the miniature actuators are fixed directly inside the wing and directly actuate the flexible upper surface of the wing, as shown in Fig. 4.

The direct actuation architecture, with estimated forces of over 1,300N per actuator, correlated with the small space inside the morphed wing (the wing thickness varies between 10cm and 20cm), and with small maximum displacement (maximum 5mm) imposed serious size/power constraints to the actuators. As there was no actuator on the market that could fit directly inside the morphing wing model and provide the right forces, the project structural team resorted to the manufacture of a dedicated actuator that fulfils these specific requirements. Therefore, the complete electro-mechanical miniature actuator was designed in-house, by using some components acquired on the market such as the miniature brushless direct current (BLDC) motor.

This approach will be very advantageous for aviation because the developed actuators, presented in this paper, are lightweight and have low power consumption (only 15watts). Because of its small size, this actuator belongs to the category of miniature actuators.

The studies presented in the paper refers to the open loop architecture of the morphing wing, focusing on the modelling, simulation and control of the actuator used in this project to control the wing shape.

3.0 ACTUATOR MODELLING AND SIMULATION

3.1 Actuator modelling

An actuator can be defined as a system capable of changing the configuration of another system when it receives a command. The design and simulation are focused on the following parts: the electrical motor, the gearbox, the gearing and the trapezoidal screw. The gearing and the trapezoidal screw are inside the actuator. The electrical motor used by the actuat or is a miniature brushless direct current (BLDC) motor. This type of motor is known for its numerous advantages, including small size and high torque. Today, the tendency is to replace brush direct current motors with this type of motor. Much research and several studies have been done on BLDC theory(44-50).

The equivalent circuit of a BLDC motor is illustrated in Fig. 6, while the associated equations are:

$$V_1 = R_1 i_1 + L_1 \frac{\mathrm{d}i_1}{\mathrm{d}t} + E_1 \qquad \ldots (1)$$

$$V_2 = R_2 i_2 + L_2 \frac{\mathrm{d}i_2}{\mathrm{d}t} + E_2 \qquad \ldots (2)$$

$$V_3 = R_3 i_3 + L_3 \frac{\mathrm{d}i_3}{\mathrm{d}t} + E_3 \qquad \ldots (3)$$

where R_1, R_2, R_3 are the windings resistances, L_1, L_2, L_3 are the windings inductances and E_1, E_2, E_3 are the induced voltages (back EMF).

The stator windings of the BLDC motor used in this application are star connected. The motor's neutral point is not accessible, therefore, the phase-to-neutral voltage cannot be measured. The mathematical model proposed in this paper uses line-to-line voltage, defined as the voltage differences between two phase-to-neutral voltages.

Subtracting Equation (1) and (2) yields:

$$V_{12} = R_1(i_1 - i_2) + L_1 \frac{\mathrm{d}(i_1 - i_2)}{\mathrm{d}t} + E_1 - E_2 \qquad \ldots (4)$$

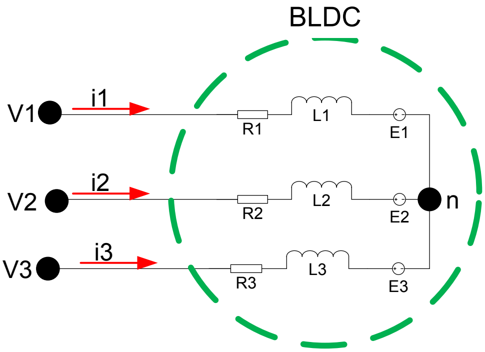

Figure 6. Motor equivalent circuit.

where $V_{12} = V_1 - V_2$, $R_1 = R_2$, and $L_1 = L_2$. Similarly, it results:

$$V_{23} = R_2(i_2 - i_3) + L_2 \frac{\mathrm{d}(i_2 - i_3)}{\mathrm{d}t} + E_2 - E_3. \qquad \ldots (5)$$

For Equations (4) and (5), it is assumed that the BLDC motor is a balanced system, which means that the BLDC motor is a symmetrical system ($R_1 = R_2 = R_3$ and $L_1 = L_2 = L_3$). In a symmetrical system with a neutral point, such as the BLDC motor, the phase currents must satisfy the next equation:

$$i_1 + i_2 + i_3 = 0 \qquad \ldots (6)$$

From Equation (6), the current of phase three (i_3) is computed as:

$$i_3 = -i_1 - i_2 \qquad \ldots (7)$$

By replacing i_3 given by Equation (7) in Equation (5) we obtain:

$$V_{23} = R_2(i_1 + 2i_2) + L_2 \frac{\mathrm{d}(i_1 + 2i_2)}{\mathrm{d}t} + E_2 - E_3 \qquad \ldots (8)$$

which can further be written as:

$$V_{23} = R_2 i_1 + 2R_2 i_2 + 2L_2 \frac{\mathrm{d}i_2}{\mathrm{d}t} + L_2 \frac{\mathrm{d}i_1}{\mathrm{d}t} + E_2 - E_3 \qquad \ldots (9)$$

From Equations (4) and (9), the motor phase currents i_1 and i_2 equations are obtained, as follows:

$$\frac{\mathrm{d}i_1}{\mathrm{d}t} = \frac{1}{3L}(2V_{12} + V_{23} - 3Ri_1 - E_{23} - 2E_{12}) \qquad \ldots (10)$$

$$\frac{\mathrm{d}i_2}{\mathrm{d}t} = \frac{1}{3L}(-V_{12} + V_{23} - 3Ri_2 - E_{23} + E_{12}) \qquad \ldots (11)$$

while the current in phase 3 is calculated using Equation (7).

When the BLDC motor is operating, the electromagnetic torque on the motor shaft is constant. To keep the torque permanently constant on the shaft, at each phase the electromotive force (back EMF) needs to be synchronised with its counterpart phase current, as indicated on the graph in Fig. 7. The induced voltage in the winding increases when the mechanical speed becomes higher. The next equation shows how the back EMF (E_1) and speed (ω) are related, and is valid for each motor phase:

$$E_1 = K_e \cdot \omega \cdot F(\theta) \qquad \ldots (12)$$

where K_e is the back EMF constant, ω is the mechanical motor speed in radians per second, and θ is the electrical rotor position. The function $F(\theta)$ in Equation (12) has a trapezoidal waveform as shown in Fig. 7, with a maximum amplitude of +1 and a minimum amplitude of –1.

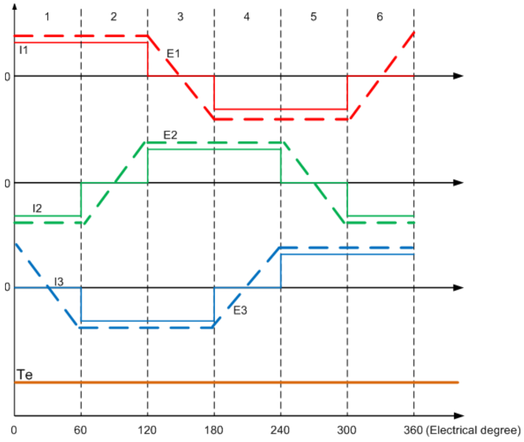

Figure 7. Phase current and back EMFs values.

The electrical power absorbed by the motor is transferred to the rotor via the air gap. This transferred power equals the sum of the products of each current and back-EMF of the three phases and is given by equation:

$$P_e = E_1 i_1 + E_2 i_2 + E_3 i_3 \qquad \ldots (13)$$

On the other way, the electromagnetic power is given by the equation below:

$$P_e = T_e \cdot \omega \qquad \ldots (14)$$

From Equations (13) and (14), it results:

$$T_e \cdot \omega = E_1 i_1 + E_2 i_2 + E_3 i_3 \qquad \ldots (15)$$

The electromagnetic torque equals the product of the torque constant and the phase current, and is written as:

$$T_e = k_t i \qquad \ldots (16)$$

where k_t is the motor torque constant. The characteristics of the BLDC motor chosen in this application are shown in Table 2.

3.2 Actuator simulation

The equations developed above (Equations (1-16)) were used with Matlab/Simulink to implement the BLDC model. Figure 8 shows the BLDC motor model with its power stage (Inverter). The Matlab/Simulink implementation of Equations (10-11) is presented in Fig. 9. This represents what occurs in the main part of the second block on the right side of Fig. 8. The power stage applies voltage to the motor's winding based on the rotor position, which is detected by a low-cost hall sensor integrated in the motor. The commutation sequence used by the power electronics to switch the power device ON and OFF (MOSFET) is presented in Fig. 10.

Table 2
Characteristics of the BLDC motor

Values at nominal voltage	
Nominal voltage	12Volts
No load speed	4,610rpm
No load current	75·7mA
Nominal speed	2,810rpm
Nominal torque (maximum continuous torque)	25·1mNm
Nominal current (maximum continuous torque)	1A
Stall torque	84·1mNm
Starting current	3·49A
Electrical characteristics	
Terminal resistance	3·43Ω
Terminal inductance	1·87mH
Torque constant	24·1mNm/A
Speed constant	397rpm/V
Mechanical time constant	20·7ms
Rotor inertia	35cm^{2}

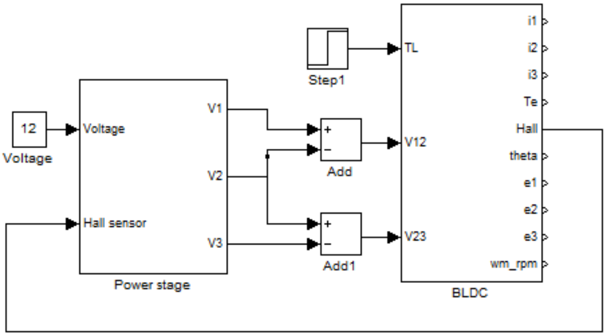

Figure 8. BLDC motor and its power stage.

Figure 11 shows the speed and torque waveforms, captured when a nominal load of $24.1\cdot10^{-3}$N·m is applied at 0·5 seconds. Figure 12 shows the phase current and the back EMF waveforms from the simulated motor model captured when the same load is applied. It is clear that the back EMF and the phase current are well-synchronised.

According to the data from Table 2, the stall torque, no load speed, nominal speed, no load current, and nominal current parameters at nominal voltage are also achieved with the designed simulation model, thus validating the proposed actuator motor simulation model.

After the numerical validation of the actuator's motor, which is the main part of the actuation system, its model (proposed in Fig. 8) is extended to obtain a complete model of the actuator. In order to model the mechanical part of the actuator, consisting of a gearbox, gearing, screw and

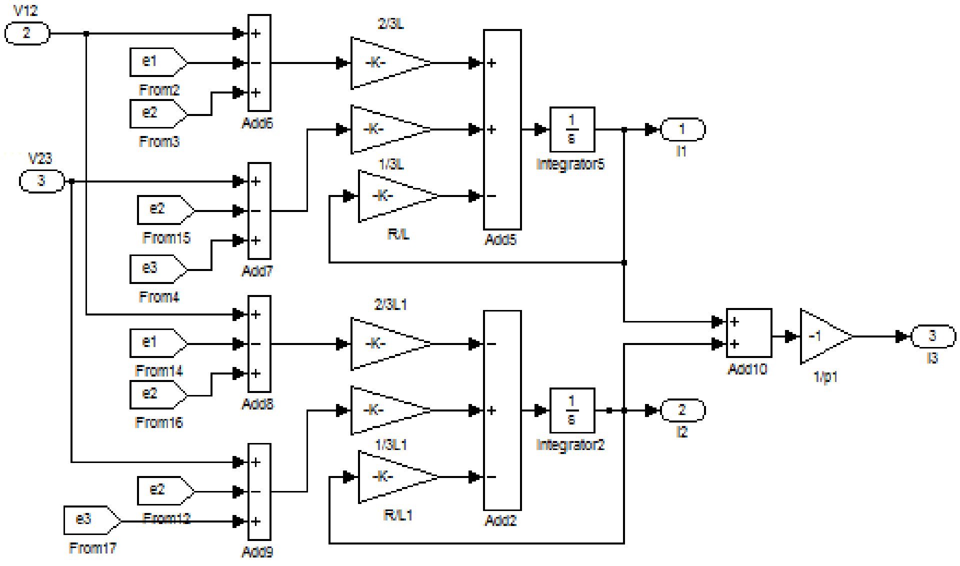

Figure 9. Simulink calculation of the phase current.

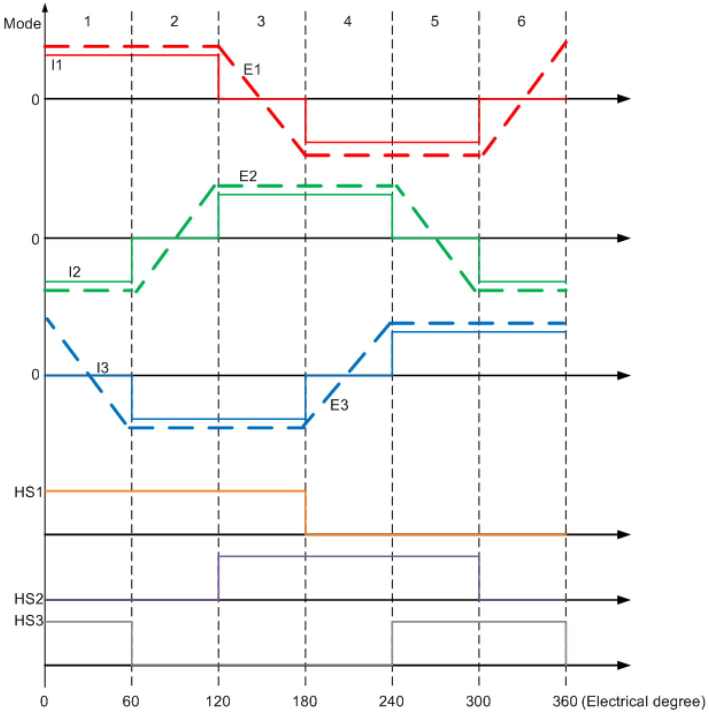

Figure 10. Commutation sequence.

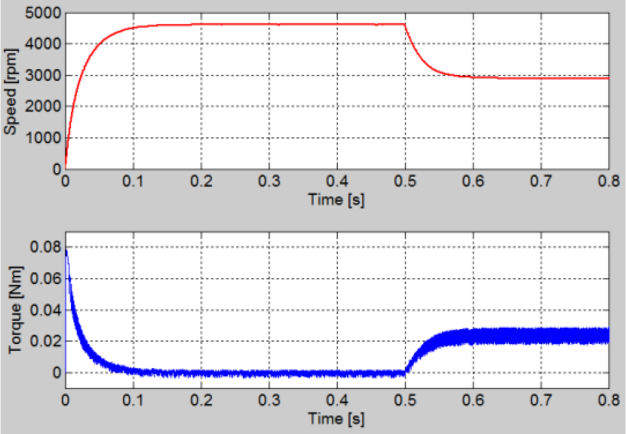

Figure 11. Speed and torque waveforms.

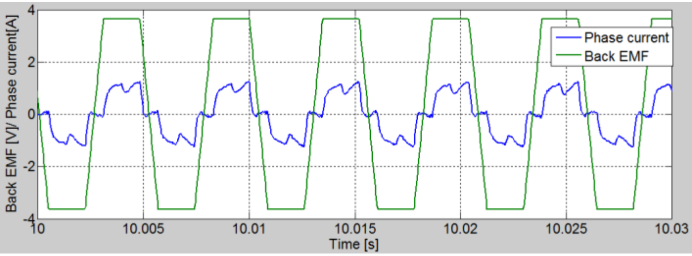

Figure 12. Current and back EMF for phase 1.

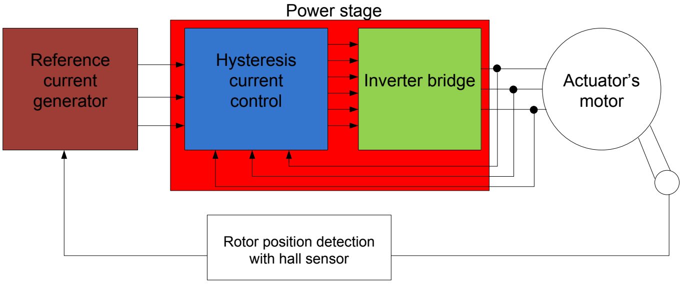

Figure 13. Actuator's current control scheme.

nut, the motor's gearbox and the gearing ratio need to be assessed. From the design structural constraints, it was assumed that for a 2mm linear displacement of the nut, the screw makes one complete mechanical revolution. A complete mechanical revolution of the screw corresponds to two revolutions of the motor's gearbox shaft.

Obviously, the actuator is modelled as an open-loop model. Open-loop (in this case) means that the actuator is powered and its output (position in millimeters) is observed without any control. The next chapter will focus on the actuator's current control as well as its position control.

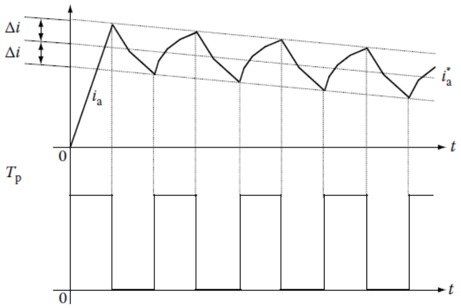

Figure 14. Illustration of the hysteresis control(49).

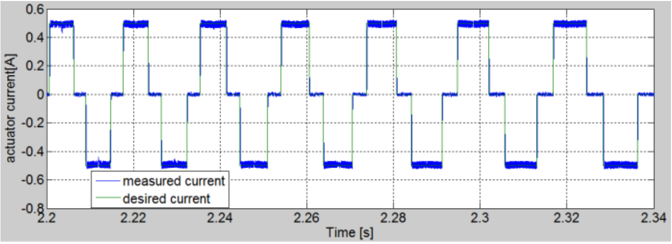

Figure 15. Simulation results with current control.

4.0 ACTUATOR CONTROL DESIGN AND NUMERICAL SIMULATION

4.1 Actuator's current control

The implementation of a current loop is useful to protect the actuator's motor against overcurrent. This loop ensures that the electromagnetic torque on the motor shaft is controlled independently of the load. The schematic of the proposed current control loop is shown in Fig. 13.

The reference current generator block generates three reference currents based on the position information from the hall sensor. Depending on the error signal between the reference and the measured current, a pulse with a modulation (PWM) signal is generated. The PWM signal is used as a firing signal for the inverter power devices. The actuator's motor is taken into account because its current is defined by the current in the motor's winding.

The power stage or inverter illustrated in Fig. 8 is extended with the current controller. The hysteresis control law for the current is implemented here because of its simplicity and accuracy. The drawback of this method is the variable switching frequency. The principle of this type of control is illustrated in Fig. 14(49). Figure 15 shows the simulation result obtained using this control technique. The current ripples visible in Fig. 15 can be reduced using a combination of a proportional-integral (PI) controller with a saw tooth signal.

4.2 Actuator's position control

A BLDC motor can be approximated as a direct current motor with brush when two phases are conducted or excited. This approximation is used to design the actuator's position control. The structure of a BLDC motor is shown in Fig. 16.

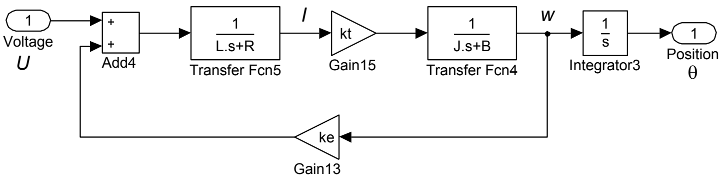

Figure 16. Structure of the BLDC motor.

To design the position control, the transfer function θ(s)/*U*(s) is used. This transfer function is derived from Fig. 16 as follows:

$$I = \frac{U - k_e w}{L \cdot \mathrm{s} + R} \qquad \ldots (17)$$

and:

$$w = \frac{k_t I}{J \cdot \mathrm{s} + B} \qquad \ldots (18)$$

From Equation (18) the motor's current yields:

$$I = \frac{w(J \cdot \mathrm{s} + B)}{k_t} \qquad \ldots (19)$$

By equalising Equation (19) with Equation (17) it results:

$$\frac{U - k_e w}{L \cdot \mathrm{s} + R} = \frac{w(J \cdot \mathrm{s} + B)}{k_t} \qquad \ldots (20)$$

Re-arranging Equation (20) we have:

$$\frac{w}{U} = \frac{k_t}{LJ \cdot \mathrm{s}^2 + RJ \cdot \mathrm{s} + k_e k_t} \qquad \ldots (21)$$

which, by considering the motor speed in revolution per minute (rpm), can be rewritten as:

$$\frac{w}{U} = \frac{30}{\pi} \cdot \frac{k_t}{LJ \cdot \mathrm{s}^2 + RJ \cdot \mathrm{s} + k_e k_t} \qquad \ldots (22)$$

From Fig. 16, we can write:

$$w = \mathrm{s} \cdot \theta \qquad \ldots (23)$$

Therefore, the transfer function (22) becomes:

$$\frac{\theta}{U} = \frac{30}{\pi} \cdot \frac{k_t}{LJ \cdot \mathrm{s}^2 + RJ \cdot \mathrm{s} + k_e k_t} \cdot \frac{1}{\mathrm{s}} \qquad \ldots (24)$$

The structure of the position control closed-loop architecture is presented in Fig. 17.

The controller used for position tracking is a proportional-derivative (PD) one because the existing integral term (I of the PID) in equation(24) eliminates the steady state error. Among the different available tuning methods(51-53), the Ziegler-Nichols method was selected, being simple

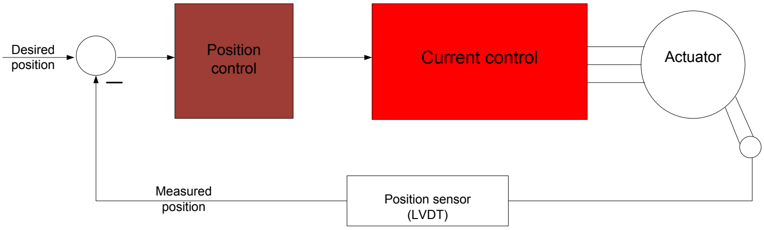

Figure 17. Structure of position control.

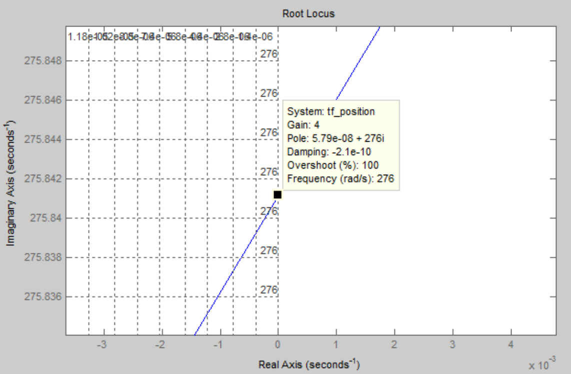

Figure 18. Zoomed view of the system’s root locus.

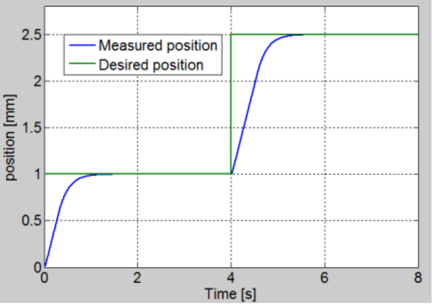

Figure 19. Simulation results obtained with the position controller.

and easy to implement. The root locus (zoomed view around the imaginary axis) of the system defined by Equation (24) is shown in Fig. 18.

From Fig. 18, the critical gain (K_c) is found to be about 4 and the oscillation period (T_c) of the system output is found to be the inverse of the frequency. Following the tuning rules proposed by Ziegler-Nichols, the coefficients of the PD controller (K_p and T_d), defined by the next equation, can be determined:

$$E(s) = K_p(1 + T_d \cdot s) \qquad \ldots (25)$$

Figure 19 shows the simulation results obtained with the position controller designed with the Ziegler-Nichols technique. The controller parameters were tuned so that no overshoot occurred.

5.0 MORPHING WING EXPERIMENTAL TEST

To develop the open loop architecture of the morphing wing system, the database of the 74 optimised aerofoils is used. Four vertical deflections (dY_{1opt}, dY_{2opt}, dY_{3opt}, dY_{4opt}) are given for each optimised aerofoil. The four displacements characterise the differences between the optimised aerofoil and the reference aerofoil in the four actuation points. In this way, the actuator designed controller should be used to control the actuators' linear positions until the real vertical displacements (dY_{1real}, dY_{2real}, dY_{3real}, dY_{4real}) of the morphing skin in the four actuation points equal the desired vertical displacements of the optimised aerofoil (dY_{1opt}, dY_{2opt}, dY_{3opt}, dY_{4opt}) corresponding to a flow condition.

The first experimental tests were performed at Ecole de Technologie Supérieure in the LARCASE facility with the physical wing model installed on the bench (Fig. 20). The architecture of the interface system between the remote computer and experimental model in the morphing wing open-loop control system is shown in Fig. 21, being made by using a National Instruments Real Time (RT) Target. The control feedback for the morphing actuators is provided by four LVDT sensors having axes parallel to the actuators' axes.

The experimental instrumentation includes: (1) a NI PXIe-1078, 9-Slot 3U PXI Express Chassis; (2) a NI PXIe-8135 embedded controller, Intel Core i7-3610QE quad-core processor (2·3GHz (base), 3·3 (single-core turbo boost)), up to 8GB/s system, up to 4GB/s slot bandwidth, 4GB (1 × 4GB DIMM) dual-channel 1,600MHz DDR3 standard, 16GB (2 × 8GB DIMM) maximum; (3) four NI PXIe-4330 data acquisition cards with Integrated Signal Conditioning for Bridge-Based Measurements, with eight simultaneously sampled analog input channels each, 25kS/s/ch sampling rate, 24-bit ADC per channel; (4) a NI PXI-8531, 1-Port CANopen Interface (up to 1 Mbit/s) for PXI; (5) a NI PXIe-6356 Simultaneous X Series Data Acquisition Card, 8 simultaneous analog inputs at 1·25MS/s/ch with 16-bit resolution, 10MS/s total AI throughput, two analog outputs, 3·33MS/s, 16-bit resolution, ±10V, 24 digital I/O lines (8 hardware-timed up to 10MHz), 4 32-bit counter/timers for PWM, encoder, frequency, event counting, and more; (6) a

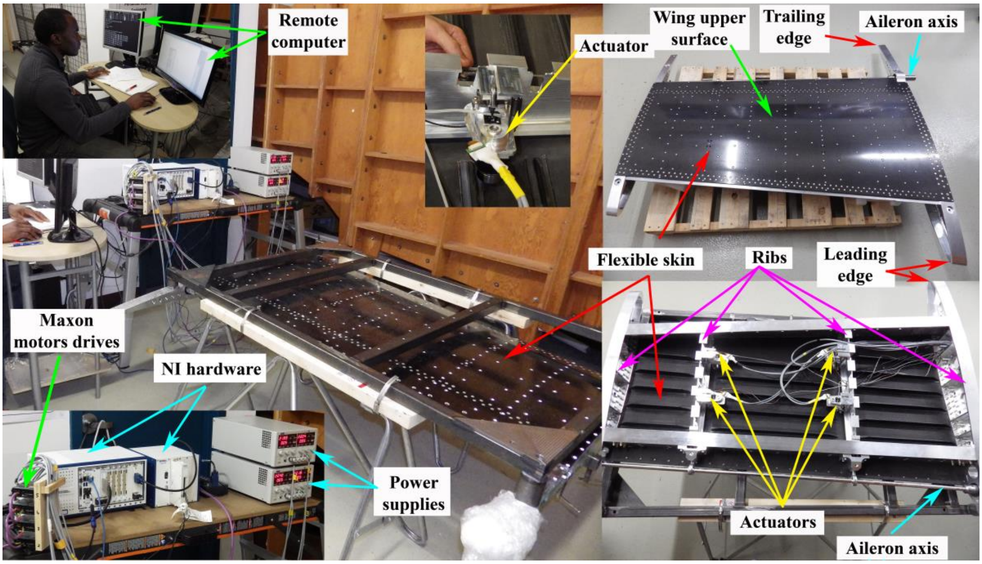

Figure 20. Bench test at LARCASE.

SCXI-1000 rugged, low-noise chassis that can hold up to four SCXI modules; (7) a NI SCXI-1540 8-Channel LVDT input module, programmable 1 or 3 Vrms excitation per channel at 2·5, 3·3, 5, or 10kHz, programmable input range per channel (0·05 to 6Vrms), 333kS/s maximum sampling rate (250Hz output bandwidth); (8) a NI SCXI-1315, 8-channel, front-mounting terminal block for the NI SCXI-1540 LVDT input module; (9) two programmable power supplies Aim-TTi CPX400DP, dual, 420watt, 60V max, 20A max.

The bench testing was a first experimental validation for the designed controller and its hardware integration architecture, and it simultaneously provided a means to observe the quality of the experimental reproducibility of the theoretical reference and optimised aerofoils. On the other way, the bench testing offers the opportunity to make some adjustments in the mechanical part of the model and some adjustments regarding the LVDT transducers zero positions. When the controller was tested on the bench two steps were performed: (1) Independent testing of the actuators – here was observed if each actuator acting independently can successfully manage the high level forces appearing under the skin morphing; (2) Simultaneous testing of the actuators. For both of these steps in bench test, was asked to the actuators to perform vertical displacements corresponding to the values ($\mathrm{d}Y_{1opt}$, $\mathrm{d}Y_{2opt}$, $\mathrm{d}Y_{3opt}$, $\mathrm{d}Y_{4opt}$) obtained for each of the 74 optimised aerofoils.

All of the bench test results were very good and proved the proper functioning of the designed control system. For example, view the results obtained for the simultaneous control of the morphing skin actuators in the Mach = 0·15, and attack angle = –1° airflow case ($\mathrm{d}Y_{1opt} = -2{\cdot}86$mm, $\mathrm{d}Y_{2opt} = 4$mm, $\mathrm{d}Y_{3opt} = -2{\cdot}53$mm, $\mathrm{d}Y_{4opt} = 3{\cdot}53$mm, aileron deflection = 5°) presented in Fig. 22. The desired values for the actuators' vertical displacements ($\mathrm{d}Y_{1opt}$, $\mathrm{d}Y_{2opt}$, $\mathrm{d}Y_{3opt}$, $\mathrm{d}Y_{4opt}$) were provided by the aerodynamic team of the project as results of the aerodynamic numerical optimisation. These values are used as reference values in the control strategy of this airflow case. The real vertical displacements of the actuators ($\mathrm{d}Y_{1real}$, $\mathrm{d}Y_{2real}$, $\mathrm{d}Y_{3real}$, $\mathrm{d}Y_{4real}$) are measured by using the LVDT position sensors equipping each actuator. The wing is considered to be optimally morphed in a flow case when the real vertical displacement equal the desired vertical displacements. The four actuators are placed on two actuation lines, at 32% (Act. #1 and Act. #3), respectively 48% (Act. #2 and Act. #4) from chord as was presented in Fig. 4.

Figure 23 confirms also the good functioning of the control system, presenting the responses of the actuation system for various repeated step signals applied as inputs for the actuators. The desired values ($\mathrm{d}Y_{1req}\,\mathrm{d}Y_{2req}\,\mathrm{d}Y_{3req}\,\mathrm{d}Y_{4req}$) were taken in order to have repeated step signals on all actuators, with positive and negative vertical displacements.

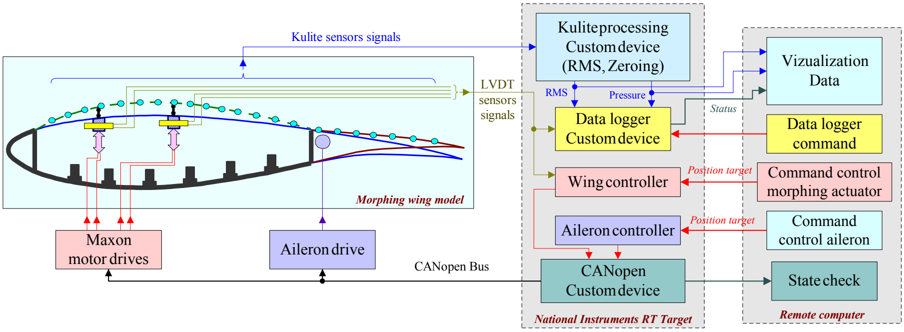

Figure 21. National Instruments RT target and remote computer configurations.

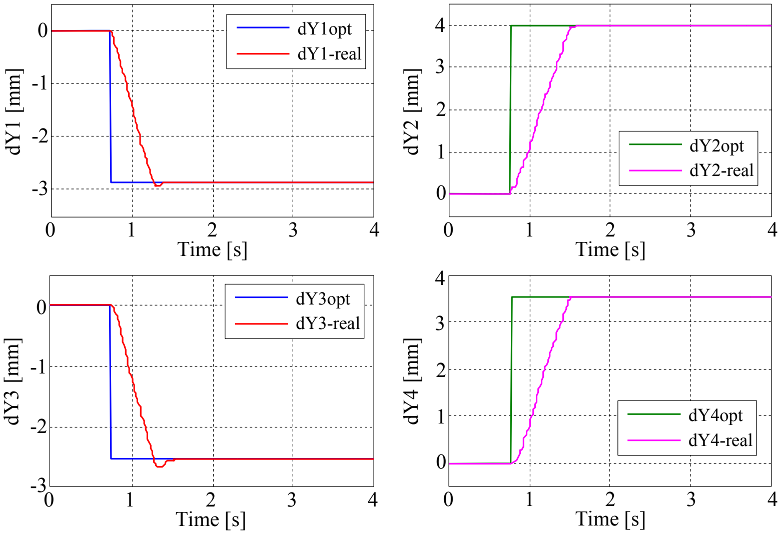

Figure 22. Bench test results for Mach = 0·15 and angle-of-attack = –1° flow case.

From the numerical values obtained for all 74 optimised aerofoil cases, it was observed that the position control absolute error due to plays in the actuators' mechanical systems, when the actuators maintain a desired position, was less than 0·1mm. These plays were fully agreed by booth structural and aerodynamic teams. From the first team point of view, the plays are important to protect the actuators in the wing bending situations, while, from the point of view of the aerodynamic team it is a safe variation because the simulation results for this wing revealed that the airflow transition point position is insensitive at deflections between –0·1mm and 0·1mm around the optimised vertical deflections of the actuators. A static loading test of the fully equipped wing, developed by the structural team, proved that the actuators were not jammed and worked properly.

The next experimental test of the morphing wing system were realised at the IAR-NRC wind tunnel by using the same instrumentation. In this first wind-tunnel test the open loop architecture of the morphing wing control system was evaluated. At this step were tested the control system of the actuators morphing the wing upper surface and the control system for the aileron deflection angle, while the pressure sensors were used just to visualise the transition point position. During this first wind-tunnel test were evaluated all optimised airflows stored in the database. The obtained results confirm the good functioning of the designed control system. Figure 24 presents the wind-tunnel test results for Mach = 0·15, and attack angle = –0·5° airflow case, while Fig. 25 describes the tracking error for all four actuators integrated in the morphing wing actuation mechanism.

Evaluating the obtained tracking errors due to the plays in mechanical parts of the actuators for this flow case resulted absolute values lower than 0·02mm. On the other way, the absolute maximal values of these kind of errors observed during all wind-tunnel tested flow cases sustain the conclusion drawn during the bench tests, being smaller than 0·1 mm. Another pertinent observation is that the actuator response was not drastically affected by the aerodynamic loads produced by the airflow in the wind-tunnel tests.

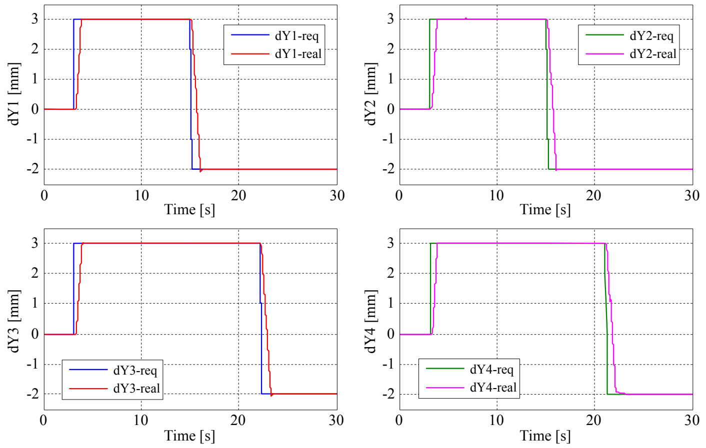

Figure 23. Bench test results for repeated step signals.

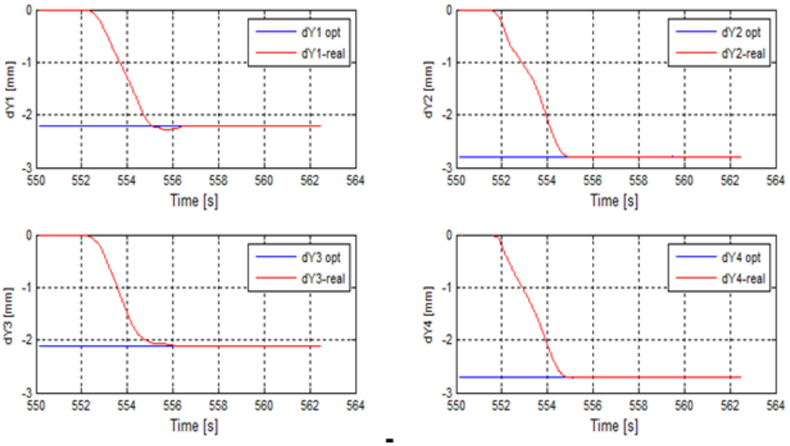

Figure 24. Wind-tunnel test results for Mach = 0·15 and angle-of-attack = –0·5°.

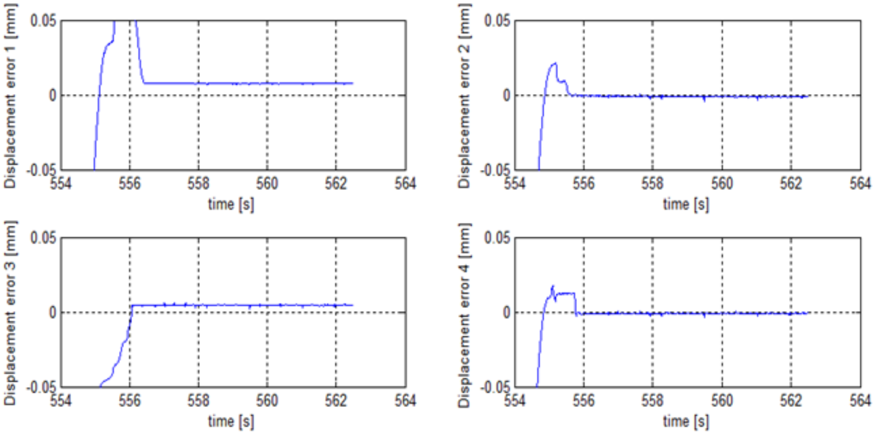

Figure 25. Displacement error (zoom) for Mach = 0·15 and angle-of-attack = –0·5° flow case.

6.0 CONCLUSIONS

The work presented here described a part of a new morphing wing application developed by using an actuation mechanism based on some miniature high-force in-house developed electrical actuators. This paper illustrated the design, simulation, and control of the miniature linear actuator used in the actuation mechanism of the morphing wing. Designed and manufactured by the structural team of the morphing wing project, the actuator consists of a miniature BLDC motor, a gearing system and a trapezoidal screw.

In order to design a control system for the actuator a preliminary modelling step is needed. Therefore, to obtain the overall model of the actuator, a model for the used BLDC motor was first designed. Its numerical validation was conducted by comparing the simulation results with the values from the motor's technical datasheet presented in Table 2. During the simulations, all parameters were achieved with the designed simulation model, thus validating the model. Further, the model was extended by adding the mechanical components. Once finalised the actuator's model, a hysteresis current controller and a position controller were developed, to control the current in the actuator and to maintain the actuator at a desired position. The controller used for position tracking was a proportional-derivative (PD) one because the existing integral term in the system mathematical model eliminated the steady state error. As tuning method, the Ziegler-Nichols method was selected, and the controller parameters were tuned so that no overshoot occurred.

At the next step four similar actuators were integrated in the actuation mechanism of the morphing wing and experimentally tested. First experimental validation for the designed controller and its hardware integration architecture was performed through bench testing at Ecole de Technologie Supérieure in the LARCASE facility, without wind blowing. Two bench testing steps were performed: (1) Independent testing of the actuators – here was observed if each actuator acting independently can successfully manage the high level forces appearing under the skin morphing; (2) Simultaneous testing of the actuators. For both of these steps in bench test, was asked to the actuators to perform vertical displacements corresponding to the optimised values obtained by the project aerodynamic team for each of the seventy-four optimised aerofoils.

The final experimental test of the open loop controlled morphing wing system were realised at the IAR-NRC wind tunnel. During this wind-tunnel test were evaluated all optimised airflows stored in the database, being tested the control system of the actuators morphing the wing upper surface and the control system for the aileron deflection angle. At this stage, the pressure sensors were used just for aerodynamic reasons, i.e. to visualise the transition point position on the wing.

Both experimental test revealed a very good behaviour of the actuation mechanism. It was observed, also, that the actuators responses were not drastically affected by the aerodynamic loads produced by the airflow in the wind-tunnel tests. From the numerical values obtained in both experimental tests for all tested optimised aerofoil cases, it was observed that the position control absolute error due to plays in actuators' mechanical systems, when the actuators maintain a desired position, was less than 0·1mm. These plays were fully agreed by booth structural and aerodynamic teams implied in the morphing wing project. From the first team point of view, the plays are important to protect the actuators in the wing bending situations, while, from the point of view of the aerodynamic team it is a safe variation because the simulation results for this wing revealed that the airflow transition point position is insensitive at deflections between –0·1mm and 0·1mm around the optimised vertical deflections of the actuators. A static loading test of the fully equipped wing, developed by the structural team, proved that the actuators were not jammed and worked properly.

ACKNOWLEDGEMENTS

The authors would like to thank for the work related to the actuator manufacturing to Professor Simon Joncas and to Master student David Barry. We would also like to thank to the Thales team for their support – mainly to Mr Philippe Molaret, Mr Bernard Blouin, and Mr Xavier Louis, and to the Bombardier Aerospace team – Mr Patrick Germain and Mr Fassi Kafyeke for their help and fruitful discussions. We would also like to thank Bombardier Aerospace, Thales, the Consortium for Research and Innovation in Aerospace in Quebec (CRIAQ), and the National Sciences and Engineering Research Council (NSERC) for the funds received on the CRIAQ MDO 505 project.

REFERENCES

1. Barbarino, S. *et al*. A review of morphing aircraft, *J Intelligent Material Systems and Structures*, 2011, **22**, (9), pp 823-877.
2. Xia, C.L. *Permanent Magnet Brushless DC Motor Drives and Controls*, John Wiley & Sons, 2012.
3. Sommerer, A., Lutz, Th. and Wagner, S. Numerical optimisation of adaptive transonic aerofoils with variable camber, Proceedings of the 22nd ICAS Congress, Harrogate, UK, 27 August – 1 September 2000.
4. Wadehn, W. *et al* Structural concepts and aerodynamic design of shock control bumps, Proceedings of the 23nd ICAS Congress, Toronto, Canada, 8-13 September 2002.
5. Sobieczky, H. and Geissler, W. Active flow control based on transonic design concepts. 17th AIAA Applied Aerodynamics Conference, Norfolk, VA, US, 28 June – 1 July 1999.
6. Sobieczky, H., Geissler, W. and Hannemann, M. Expansion shoulder bump for wing section viscous/wave drag control. IUTAM Symposium on Mechanics of Passive and Active Flow Control, Fluid Mechanics and its Applications, Göttingen, Germany, 7-11 September 1998.
7. McGowan, A.-M.R. *et al* Aeroservoelastic and structural dynamics research on smart structures conducted at NASA Langley Research Center, Proceedings of SPIE 3326, Smart Structures and Materials 1998: Industrial and Commercial Applications of Smart Structures Technologies, 16 June 1998.
8. Wlezien, R.W. *et al* The aircraft morphing program. Proceedings of SPIE 3326, Smart Structures and Materials 1998: Industrial and Commercial Applications of Smart Structures Technologies, 16 June 1998.
9. Stanewsky, E. Adaptive wing and flow control technology, *Prog Aerospace Sci*, October 2001, **37**, (7), pp 583–667.
10. Gomez, J.C. and Garcia, E. Morphing unmanned aerial vehicles, *Smart Materials and Structures*, 2011, **20**, (10), pp 1-16.
11. Elzey, D.M., Sofla, A.Y. and Wadley, H.N. A bio-inspired high-authority actuator for shape morphing structures, Proceedings of SPIE 5053, Smart Structures and Materials 2003: Active Materials: Behavior and Mechanics, 12 August 2003.
12. Weisshaar, T.A. Morphing Aircraft Technology – New Shapes for Aircraft Design. Multifunctional Structures / Integration of Sensors and Antennas. Meeting Proceedings RTO-MP-AVT-141, Overview 1. Neuilly-sur-Seine, France, 2006, pp O1-1 – O1-20.
13. Abdullah, E.J., Bil, C. and Watkins, S. Numerical simulation of an adaptive aerofoil system using SMA actuators, 48th AIAA Aerospace Sciences Meeting Including the New Horizons Forum and Aerospace Exposition, Orlando, Florida, US, 4-7 January 2010.
14. Pecora, R. *et al* Design and functional test of a morphing high-lift device for a regional aircraft, *J Intelligent Material Systems and Structures*, July 2011, **22**, pp 1005-1023.
15. Barbarino, S., Dettmer, W.G. and Friswell, M.I. Morphing Trailing Edges with Shape Memory Alloy Rods, 21st International Conference on Adaptive Structures and Technologies (ICAST), University Park, Pennsylvania, 4-6 October, 2010.
16. Song, G. and Ma, N. Robust control of a shape memory alloy wire actuated flap, *Smart materials and Structures*, 2007 **16**, (6), pp N51-N57.
17. Benavides, J.C. and Correa, G. Morphing wing design using nitinol wire, 2004, *Intelligent Systems Center Research J*, **3**, (1), pp 1-39.
18. Seow, A.K., Liu, Y. and Yeo, W.K. Shape Memory Alloy as Actuator to Deflect a Wing Flap, Proceedings of the 16th AIAA/ASME/AHS Adaptive Structures Conference, Schaumburg, IL, US, 7-10 April 2008, pp 1-11.

19. Mason, W.H., Robertshaw, H. and Inman, D.J. Recent experiments in aerospace and design engineering education, 42nd AIAA Aerospace Sciences Meeting and Exhibit, Reno, Nevada, US, 5-8 January 2004.
20. Barbarino, S. *et al* Aerofoil morphing architecture, based on shape memory alloys, ASME 2008 Conference on Smart Materials, Adaptive Structures and Intelligent Systems Smart Materials, Adaptive Structures and Intelligent Systems, Ellicott City, Maryland, US, 28–30 October 2008.
21. Abdullah, E.J., Bil, C. and Watkins, S. Application of smart materials for adaptive aerofoil control, 47th AIAA Aerospace Sciences Meeting Including the New Horizons Forum and Aerospace Exposition, Orlando, Florida, US, 5-8 January 2009.
22. Abdullah, E.J., Bil, C. and Watkins, S. Adaptive aerofoil control system using shape memory alloy actuators for unmanned aerial vehicles, Proceedings of the 21st Australasian Conference on the Mechanics of Structures and Materials: Incorporating Sustainable Practice in Mechanics of Structures and Materials, AK Leiden, The Netherlands, 7-10 December 2010, pp 141-146.
23. Abdullah, E.J., Bil, C. and Watkins, S. Performance of Adaptive Aerofoil Control System Using Shape Memory Alloy Actuators for UAV, 11th AIAA Aviation Technology, Integration, and Operations (ATIO) Conference, Virginia Beach, VA, US, 20-22 September, 2011.
24. Hutapea, P. *et al*. Development of a smart wing, *Aircraft Engineering and Aerospace Technology*, 2008, **80**, (4), pp 439-444.
25. Botez, R. M., Molaret, P. and Laurendeau, E. Laminar Flow Control on a Research Wing Project Presentation Covering a Three Year Period, CASI Aircraft Design and Development Symposium, Toronto, Canada, 24-26 April 2007.
26. Allison, D.O. and Dagenhart, J.R. Design of a laminar-flow-control supercritical aerofoil for a swept wing, CTOL Transport Technology, NASA Langley Research Center, 1978, pp 395-408.
27. Tutty, O.R., Hackenberg, P. and Nelson, P.A. Numerical optimisation of the suction distribution for laminar flow control, *AIAA J*, 2008, **38**, (2), 2000, pp 370-372.
28. Pralits, J.O. Optimal design of natural and hybrid laminar flow control on wings, Technical Reports from Royal Institute of Technology, Department of Mechanics, SE-100 44, Stockholm, Sweden, October 2003.
29. Rioual, J.-L., Nelson, P.A. and Fisher, M.J. Experiments on the automatic control of boundary-layer transition, *J Aircraft*, 1994, **31**, (6), pp 1416-1418.
30. Dimino, I., Flauto, D., Diodati, G., Concilio, A. and Pecora, R. Actuation system design for a morphing wing trailing edge, *Recent Patens on Mechanical Engineering*, 2014, **7**, pp 138-148
31. Pecora, R., Magnifico, M., Amoroso, F. and Monaco, E. Multi-parametric flutter analysis of a morphing wing trailing edge, *Aeronaut J*, 2014, **118**, (1207), pp 1063-1078
32. Pecora, R., Amoroso, F., Amendola, G. and Concilio, A. Validation of a smart structural concept for wing-flap camber morphing, *Smart Structures and Systems*, 2014, **14**, (4), pp 659-678
33. Popov, A.V. *et al* Closed-loop control simulations on a morphing wing, *J Aircraft*, 2008, **45**, (5), pp 1794-1803.
34. Grigorie, T.L. *et al* Smart concepts for actuation system and its control in a morphing wing, Proceedings of the XXXIInd Caius Iacob National Conference on Fluid Mechanics and its Technical Applications, Bucharest, Romania, 29-30 September 2011.
35. Grigorie, T.L. *et al* On–off and proportional–integral controller for a morphing wing. Part 1: Actuation mechanism and control design, *Proceedings of the Institution of Mechanical Engineers, Part G: J Aerospace Engineering*, 2012, **226**, (2), pp 131-145.
36. Grigorie, T.L. *et al* On-off and proportional–integral controller for a morphing wing. Part 2: Control validation–numerical simulations and experimental tests, *Proceedings of the Institution of Mechanical Engineers, Part G: J Aerospace Engineering*, 2012, **226**, (2), pp 146-162.
37. Grigorie, T.L. *et al* A hybrid fuzzy logic proportional-integral-derivative and conventional on-off controller for morphing wing actuation using shape memory alloy. Part 1: Morphing system mechanisms and controller architecture design, *Aeronaut J*, 2012, **116**, (1179), pp 433-449.
38. Grigorie, T.L. *et al* A hybrid fuzzy logic proportional-integral-derivative and conventional on-off controller for morphing wing actuation using shape memory alloy, *Part 2: Controller implementation and validation, Aeronaut J*, 2012, **116**, (1179), pp 451-465.
39. Grigorie, T.L. and Botez, R.M. Adaptive neuro-fuzzy inference system-based controllers for smart material actuator modelling, Proceedings of the Institution of Mechanical Engineers, *Part G: J Aerospace Engineering*, 2009, **223**, (6), pp 655-668.
40. Grigorie, T. and Botez, R.M. New adaptive controller method for SMA hysteresis modelling of a morphing wing, *Aeronaut J*, 2010, **114**, (1151).

41. NEAL, D., AKLE, B. and HESSE, T. Optimal flight control of an adaptive aircraft wing modelled by Neuro Fuzzy techniques, 2003 IEEE International Symposium on Intelligent Control, Houston, TX, US, 5-8 October 2003, pp 364-370.
42. KAMMEGNE, M.J.T. *ET AL* Design and Validation of a Position Controller in the Price-Païdoussis Wind Tunnel. The 33rd IASTED International Conference on Modelling, Identification and Control (MIC 2014), Innsbruck, Austria, 17-19 February 2014.
43. MOSBAH, A.B. *ET AL* New methodology for wind tunnel calibration using neural networks-EGD approach, *SAE Int J Aerospace*, 2013, **6**, (2), pp 761-766.
44. KRISHNAN, R. *Electric motor drives: modelling, analysis, and control*, Prentice Hall, 2001.
45. MOHAN, N. *Power Electronics: A First Course*, Wiley, 2012.
46. IRWIN, J. *ET AL* *Control in Power Electronics: Selected Problems*, Academic press, 2002.
47. LEONHARD, W. *Control of Electrical Drives*, Springer, 2001.
48. BISHOP, R.H. and DORF, R.C. *Modern control systems*, Prentice Hall College Division, 2004.
49. KRISHNAN, R. *Permanent Magnet Synchronous and Brushless Dc Motor Drives*, CRC press, 2010.
50. BALDURSSON, S. BLDC Motor Modelling and Control-A Matlab®/Simulink® Implementation, Master thesis, Electrical Power Engineering Department, Institutionen för Energi och Miljö, 2005.
51. KATSUHIKO, O. *Modern control Engineering*, Prentice Hall, 2010.
52. KATSUHIKO, O. *Matlab for Control Engineers*, Prentice-Hall, 2007.
53. PARASKEVOPOULOS, P. *Modern Control Engineering*, CRC Press, 2001.